Flat-top silver nanocrystals on the two polar faces of ZnO: An all angle x-ray scattering investigation

Nathalie Jedrecy,[1] Gilles Renaud,[2] Rémi Lazzari,[3] and Jacques Jupille[3]
[1]*Laboratoire de Minéralogie-Cristallographie, Universités Pierre et Marie Curie et Denis Diderot, CNRS UMR 7590, 4 Place Jussieu, 75252 Paris Cedex 05, France*
[2]*CEA-Grenoble, Département de Recherche Fondamentale sur la Matière Condensée, Service de Physique des Matériaux et Microstructures, Nanostructures et Rayonnement Synchrotron, 17 Avenue des Martyrs, 38054 Grenoble, Cedex 9, France*
[3]*Groupe de Physique des Solides, CNRS UMR 7588, Universités Paris 6 et 7, Campus Boucicaut, 140 Rue de Lourmel, 75015 Paris, France*

(Received 15 December 2005; revised manuscript received 28 February 2005; published 14 July 2005)

The growth of silver at room temperature on the two polar faces of ZnO, (0001) Zn terminated and $(000\bar{1})$ O terminated, has been investigated *in situ* by using grazing incidence x-ray diffraction and grazing incidence small angle x-ray scattering (GISAXS). On both surfaces, silver forms nanoclusters with (111) top facets in hexagon-on-hexagon epitaxy with $[10\bar{1}]_{Ag}\|[100]_{ZnO}$. Despite the high lattice mismatch in the latter direction (-11%), the Ag islands adopt their bulk parameter even at the very beginning of the growth, a key feature assigned to a quasi-perfect coincidence of a 9×9 Ag cell on a 8×8 ZnO cell. The GISAXS patterns give evidence of triangular and hexagonal cluster shapes on the Zn and O surfaces, respectively, which reflect the topographies of the two surfaces. Quantitative analysis is performed to deduce the morphological parameters as a function of coverage. To represent highly covered surfaces involving large clusters with complex shapes, a specific GISAXS treatment in terms of holes in a continuous metal layer is proposed. In the O case, flat-top islands develop mostly laterally until an incompletely filled thick layer is formed. In the Zn case, the islands grow both in height and in diameter until the film can be represented by a layer with holes. The derived growth parameters attest that silver spreads significantly better on the O-terminated face than on the Zn termination.

DOI: 10.1103/PhysRevB.72.045430 PACS number(s): 61.10.Eq, 61.10.Nz, 68.35.Ct, 68.55.Ac

I. INTRODUCTION

The oxides and their interplay with metals are of central importance in environmental and earth science as well as in technological applications.[1,2] The latter include catalysts, gas sensors, and optical, electronic, or magnetic devices. Systems based on the zinc oxide, which exhibits various physical (direct band gap in the UV region, high exciton binding energy) and chemical (mixing of covalent-ionic characters, high solubility of group III impurities and of transition metal ions) properties,[3] are among those which have considerable potential in all fields. Applications of particular relevance concern noble metals supported on ZnO. Copper on ZnO is employed on industrial scale for methanol synthesis and water-gas shift reaction.[4] Silver on ZnO is used in low-emissive and antisolar coatings on glasses.[5,6] A central concern in manufacturing the coatings is the way the silver film, which is expected to behave as a perfect mirror in the infrared wavelength range, wets its oxide support.

Vapor-deposited metals grow generally on oxide surfaces in the form of three-dimensional (3D) nanometer-sized clusters rather than in a monolayer-by-monolayer mode.[7,8] A variety of parameters are involved in the growth process (the electronic and crystalline structures of the two materials, the respective surface free energies, the interface energy, kinetic factors), determining the atomic structure, the shape, and the size of the metallic clusters. The nanoclusters morphology and the statistical organization on the substrate determine in turn the physical and reactive properties of the overall system.[9,10] The peculiarity of noble and late transition metals on the basal planes of zinc oxide, namely the (0001) Zn-terminated and the $(000\bar{1})$ O-terminated surfaces, is that their growth proceeds with an enhanced two-dimensional character. The critical coverage, defined as the fraction of the surface covered by the metal at the onset of the formation of the second atomic layer, has been estimated to 1 for platinum[11–13] and to 0.55 (Ref. 14) (0.35)[15] for copper on O (Zn) face. In the case of copper, flat-top clusters are formed.[14,16] A pseudo layer-by-layer growth has been inferred, tentatively explained by either purely kinetic mechanisms[14] or electronic transfer process from metal to surface states.[17]

The practical importance of the ZnO-supported Ag films, together with the fundamental questions regarding adhesion of metals on oxide polar surfaces, have prompted us to undertake an x-ray study of the growth of silver on the two unreconstructed polar faces of ZnO. The use of x rays enables one to follow the metal/oxide growth, averaged over the whole surface, *in situ* and in a nondestructive way, from 0.2 to 3.4 nm of equivalent thickness. Morphological and structural features are derived in a combined way from grazing incidence x-ray scattering, at small and large emergence angles, respectively. Grazing incidence x-ray diffraction (GIXD) probes the order at the atomic scale. Grazing incidence small-angle x-ray scattering (GISAXS) probes the morphology and the spatial distribution of nanometer-sized objects.[18–20] The instrument used herein has benefited from recent developments to analyze, *in situ* and quasi in real time, particles grown on surfaces in UHV environment.[21] It allows an exact knowledge of the metal/oxide interface struc-

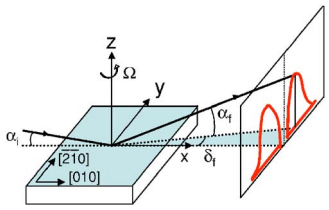

FIG. 1. (Color online) Geometry of the GISAXS measurements, in which the *X*, *Y*, *Z* axes are fixed in the laboratory frame. The x-ray beam falls on the surface under a grazing angle α_i. The orientation of the in-plane axes of the sample is determined by the value of the rotation angle Ω around the surface normal ($\Omega=0°$ for $[010]\|X$ axis). The intensity scattered along any direction characterized by out-of-plane and in-plane angles, α_f and δ_f respectively, is collected on a CCD camera, fixed at reasonable distance from the sample, perpendicularly to the *X* axis.

ture both at nanoscopic and mesoscopic scale. This is a prerequisite if one wants to be able in future to tune chemical adsorption properties of supported systems (catalysis), or optical/magnetic properties of nanocomposite materials.

II. EXPERIMENTS

The geometry of the GISAXS measurements is shown in Fig. 1. The incident x-ray beam of wave vector $\mathbf{k_i}$ makes an angle α_i with the surface. The orientation of the principal axes of the sample with respect to $\mathbf{k_i}$ is determined by the rotation angle Ω around the surface normal ($\Omega=0°$ for $[010]_{\mathrm{ZnO}}$ parallel to the X axis). Grazing incidence geometry maximizes the surface signal to noise ratio. The x-ray beam is scattered by the assembly of supported particles along directions $\mathbf{k_f}$ determined by the out-of-plane and in-plane angles, α_f and δ_f, respectively. In the present work, these angles were ranging between 0° and 5.4° for α_f and between −1.9° and 3.5° for δ_f. Even if it does not describe entirely the scattering process at small angles (see Appendix A), we will use in figures the scattering wave vector $\mathbf{q}=\mathbf{k_f}-\mathbf{k_i}$ given by

$$q_x = k_0[\cos(\delta_f)\cos(\alpha_f) - \cos(\alpha_i)],$$

$$q_y = k_0[\sin(\delta_f)\cos(\alpha_f)],$$

$$q_z = k_0[\sin(\alpha_f) + \sin(\alpha_i)], \qquad (2.1)$$

where $k_0=2\pi/\lambda$ with λ being the x-ray wavelength. The same geometry is used for GIXD except that the scattering centers are the atoms and that the two outgoing angles α_f, δ_f may vary between 0° and 90°.[22]

The experiments were performed at the European Synchrotron Radiation Facility (ESRF) using the UHV surface diffraction setup of the CRG BM32 beamline.[23] A doubly focused x-ray beam of 18 keV was used, with a typical 0.4 $\times$0.3 mm^2 horizontal times vertical size. The angle α_i was fixed at the critical angle of ZnO for total external reflection: $\alpha_c=0.155°$. The GISAXS scattering was measured using a charge coupled device (CCD) detector, at fixed position 680 mm downstream the sample center. The active window of the CCD camera, perpendicular to the in-plane x-ray direction (*X* axis), is made of 1242 and 1152 pixels along the in-plane *Y* axis and the out-of-plane *Z* axis, respectively, with a pixel size of 56.25 μm. The resolution in reciprocal space units was thus about 0.0075 nm^{-1}. The transmitted and specularly reflected x-ray beams were hidden by purposely designed beam stops and antiscattering slits.[24] The δ_f lower acceptance was ±0.086° (that is $q_y=\pm0.14$ nm^{-1}). A standard scintillator detector, which could be positioned in the direction of any $\mathbf{k_f}$, was used for the measurement of GIXD intensities.

The ZnO substrates were commercial hydrothermally grown single crystals with (0001) or $(000\bar{1})$ orientations. The clean (1×1) surfaces have been obtained after several cycles of sputtering with 0.6–1.5 keV Ar^+ and annealing at 1000 K in UHV followed by cooling down under O_2 pressure (10^{-5} mbar). Silver was evaporated using a resistively heated Knudsen cell, the substrate being kept at room temperature. The used flux of 0.062 nm/min was calibrated with a quartz microbalance. On the basis of this calibration and assuming a similar sticking coefficient on the microbalance and on the ZnO substrates, a deposited amount could be determined for the Ag/ZnO films. It is expressed in nanometers.

III. EPITAXY AND CRYSTALLINE ANALYSIS

ZnO crystallizes in the wurtzite structure which consists in the stacking of atomic layers composed either by O anions or Zn cations, with in-plane hexagonal symmetry. The layers are stacked according to the sequence *AaBbAa*… where *A*, *B* refer to Zn and *a*, *b* to O. The *Aa* and *aB* interlayer spacings are equal to 0.199 and 0.061 nm, respectively. The truncation perpendicular to the *c* axis arises between *A* and *a* layers (or between *B* and *b*), leading on the one side to a Zn-terminated (0001) surface and on the other side to an O-terminated $(000\bar{1})$ surface. The two polar surfaces are stabilized under UHV while preserving a (1×1) bulklike order. The stabilization mechanisms are however depending on the chemical nature of the surface.[25] On the Zn-terminated surface, the dipole moment is compensated via a change in stoichiometry. The average concentration of Zn atoms is reduced by 1/4 in the outermost layer. This change in stoichiometry is not generated by a random distribution of vacancies but by one bilayer high triangular islands (*bA*) or one bilayer deep triangular holes.[26] On the contrary, the outermost layer of the O-terminated surface is found to be stoichiometric and flat;[16,27] a partial charge transfer from the O surface anions towards the bulk may be inferred. Silver crystallizes in the fcc structure. Considering the (111) planes of in-plane hexagonal symmetry, the expected lattice mismatch with ZnO(0001)-Zn [or $(000\bar{1})$-O] is equal to −11% along the natural $[10\bar{1}]_{\mathrm{Ag}}\|[100]_{\mathrm{ZnO}}$ azimuth. A rotation by 30° of the in-plane hexagonal cell of Ag with respect to that of ZnO leads to a lattice mismatch of +2.75% ($[10\bar{1}]_{\mathrm{Ag}}\|[210]_{\mathrm{Ag}}$ azimuth).

Scans performed in various regions of the reciprocal

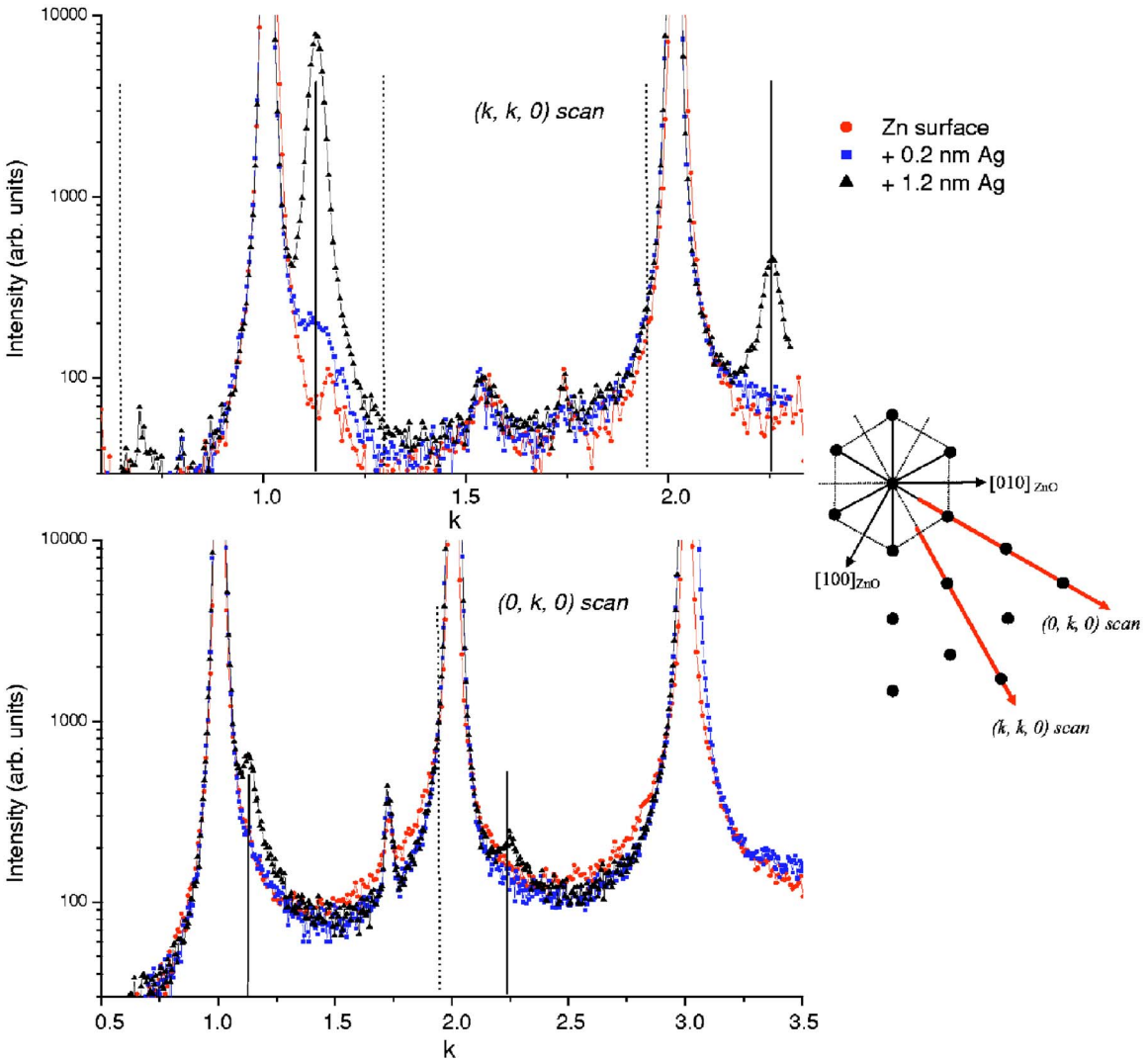

FIG. 2. (Color online) Typical in-plane scans before and after 0.2 or 1.2 nm Ag deposit on the Zn0(0001) Zn-terminated surface. The solid (dashed) vertical lines indicate the peak positions expected for the Ag(111) epitaxy with lattice mismatch of −11% (+2.75%). A schematic top view of the ZnO in-plane reciprocal space is shown aside.

space (RS) during the growth of the Ag film showed the occurrence of a unique $[10\bar{1}]_{\mathrm{Ag}}\|[100]_{\mathrm{ZnO}}$ epitaxy (epitaxy I) on the two basal surfaces prepared under state-of-the-art conditions (that is with ion bombardment and further annealing to improve the cristallinity). We briefly mention that, on ill-crystallized surfaces (not in the present work), we have detected the $[10\bar{1}]_{\mathrm{Ag}}\|[210]_{\mathrm{ZnO}}$ epitaxy (epitaxy II) as a minority structure at low coverage. Any RS location is referred to by use of the coordinates (h,k,L) of the momentum transfer vector $\mathbf{q}=\mathbf{k}_f-\mathbf{k}_i$ in the $(\mathbf{a}^\star,\mathbf{b}^\star,\mathbf{c}^\star)$ basis associated with the hexagonal ZnO $(\mathbf{a},\mathbf{b},\mathbf{c})$ unit cell. Typical in-plane scans actually performed at $L=0.06$ are shown in Fig. 2. They were recorded on the clean ZnO(0001)-Zn surface and after deposition of 0.2 and 1.2 nm of silver. The peaks at $k=1.54$ and $k=1.73$ in the $(k,k,0)$ scan, as well as the peak at $k=1.73$ in the $(0,k,0)$ scan, are already present on the clean surface. They thus do not affect the interpretation. Except for the peak at $k=1.54$, they are due to stacking faults inside the bulk ZnO crystal. The Ag signal is clearly detected at all coverages, at $k=1.124$ in the $(k,k,0)$ scan. This signal corresponds (epitaxy I) to an in-plane bulk Ag reflection, the $02\bar{2}$ reflection if one refers to the fcc lattice. In the case of epitaxy II, the same reflection would show up at $k=1.946$ in the $(0,k,0)$ scan. Importantly, silver adopts its own lattice parameter from the very beginning of the growth. In the $(0,k,0)$ scan, the signal at $k=1.124$ is one order of magnitude weaker, since it arises from diffuse scattering along the normal direction or, in other words, from a Ag crystal truncation rod (CTR). The CTR attests to the flatness of the interfaces of silver with vacuum and with ZnO. The lateral coherent domain size can be estimated from the width of the in-plane scans by assuming a perfect alignment of the Ag crystalline domains with the ZnO in-plane axes. On the Zn-terminated surface, it is found equal to about 2 nm at the beginning of the growth (deposited amount of 0.2 nm) and to about 10 nm for the higher thickness investigated (3.4 nm).

A cut of the RS perpendicular to $[100]_{\mathrm{ZnO}}$ is shown schematically in Fig. 3(a), in the assumption of a ABCA… stack-

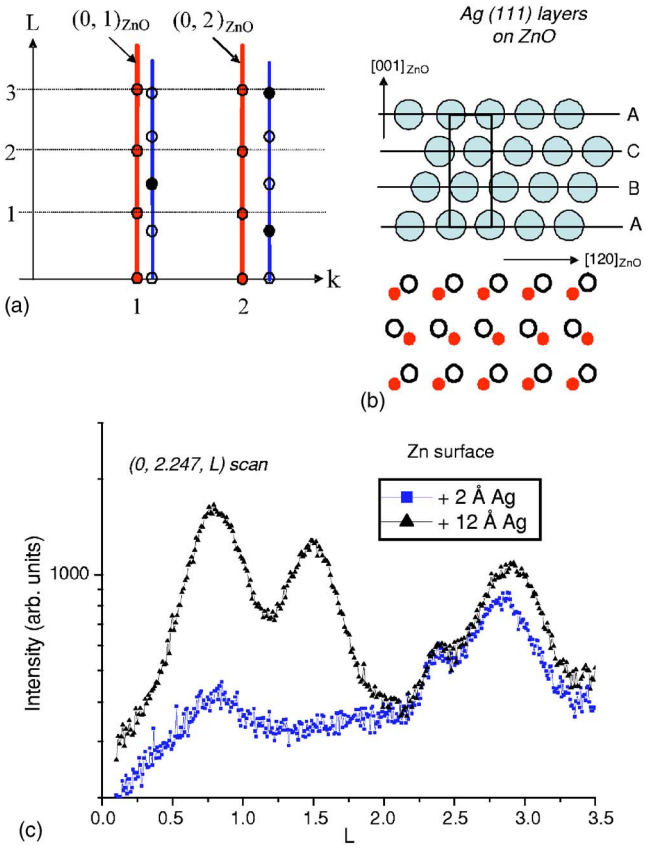

FIG. 3. (Color online) (a) Cross section of the reciprocal space perpendicular to $[100]_{ZnO}$, showing ZnO and Ag crystal truncation rods, in the assumption of a single type of fcc staking for Ag. Full circles indicate Bragg positions whereas open ones correspond to fcc forbidden reflections. (b) Cross section of the corresponding Ag/ZnO system. Large gray circles are Ag atoms, small solid (open) circles are zinc (oxygen). (c) Out-of-plane L scans along a second-order Ag rod, after 0.2 and 1.2 nm deposit.

ing for (111) Ag planes. The ZnO and Ag CTRs are displayed together with bulk-type reflections indicated by full circles, whereas forbidden reflections are shown in the form of open circles. Figure 3(b) is the corresponding real space representation. Some out-of-plane scans, along the Ag CTR of type $(h,k)=(2,0)$, are shown in Fig. 3(c). The presence of the peak at $L=0.73$, once 0.2 nm of silver is deposited, demonstrates that, at this early stage of the growth, the islands already involve at least three atomic (111) layers (the interlayer spacing is 0.236 nm). Note that at $L=2.94$, Ag contribution is mostly hidden by the bulk ZnO reflection at $L=3$. An extra peak is recorded at $L=1.47$ which is due to the presence of silver (111) planes stacked according to a reverse sequence ACBA… relative to that chosen in Fig. 3(b). Such sequence is also retrieved by a rotation of 60° (or 180°) around the surface normal. The signals from the two stacking rapidly become (1.2 nm coverage) of the same intensity. Due to the 6 mm ZnO surface symmetry,[25] the formation during the growth of twin crystallites in similar amounts seems more likely than the occurrence of stacking faults.

IV. MORPHOLOGY OF THE AG/ZNO FILM

A. Diffuse x-ray scattering at small angles: Theoretical background

This section is aimed at describing the main ingredients used in the calculation of the intensity scattered at small angles by an assembly of particles in a host medium. In the present case, particles are Ag islands supported on ZnO surfaces. They are treated as a perturbation in the propagation of the x-ray wave field on top of the substrate. A complementary approach, being more relevant when dealing with an incompletely filled thick layer, is to consider that the scattering entities are holes between islands. The two models will be used herein. The total scattering cross section[28] for an assembly of scatterers n located at $\mathbf{r}_{n,\parallel}$ reads

$$\left(\frac{d\sigma}{d\Omega}\right)_{tot} \propto \sum_n |\mathcal{F}_n|^2 + \sum_n \sum_{m\neq n} \mathcal{F}_n \mathcal{F}_m^{\star} e^{i\mathbf{q}_{\parallel}\cdot(\mathbf{r}_{n,\parallel}-\mathbf{r}_{m,\parallel})}, \quad (4.1)$$

where $\mathcal{F}_n(\mathbf{k}_i,\mathbf{k}_f)$ is a kind of Fourier transform of the electronic density of the particle n (island or hole), through its average shape. In fact, $\mathcal{F}_n$, the so-called form factor, includes multiple reflection effects by the substrate or by the possibly constituted vacuum-layer interface, due to the closeness of the out-of-plane angles α_i, α_f and of the critical angle α_c for total external reflection. The detailed formalism for computing $\mathcal{F}_n$ within the distorted wave born approximation (DWBA)[29] is given in Appendix A. For a homogeneous ergodic system, the spatial average that should be applied to Eq. (4.1) due to the finite beam coherence length is replaced by a configuration average over all possible situations, introducing the probability p_X for a particle to be of type X (the shape and size are fully determined by the particle type X) and the probability $p_Y G_{Y|X}(\mathbf{r}_{n,\parallel},\mathbf{r}_{m,\parallel})$ to have a particle of type Y at vector $\mathbf{r}_{m,\parallel}$, knowing the particle at vector $\mathbf{r}_{n,\parallel}$ is of type X. The function $G_{Y|X}(\mathbf{r}_{n,\parallel},\mathbf{r}_{m,\parallel})$ is the partial pair correlation function between X and Y. The intensity is written as:

$$\left(\frac{d\sigma}{d\Omega}\right)_{tot} \propto \sum_X p_X|\mathcal{F}_X|^2 + \sum_X \sum_Y \mathcal{F}_X \mathcal{F}_Y^{\star} \times \int\int_{n\neq m} d^2r_n d^2r_m p_X p_Y G_{Y|X}(\mathbf{r}_{n,\parallel},\mathbf{r}_{m,\parallel}) e^{i\mathbf{q}_{\parallel}\cdot(\mathbf{r}_{n,\parallel}-\mathbf{r}_{m,\parallel})}, \quad (4.2)$$

the integration being done over the whole surface.

At this stage, two types of approximation are usually encountered. The first one is known as the decoupling-approximation (DA);[28] it assumes that $G_{Y|X}(\mathbf{r}_{n,\parallel},\mathbf{r}_{m,\parallel})$ does not depend on the particle types but only on the relative distance between scatterers, i.e., $G_{Y|X}(\mathbf{r}_{n,\parallel},\mathbf{r}_{m,\parallel})=G(\mathbf{r}_{n,\parallel}-\mathbf{r}_{m,\parallel})$. The intensity may be written as the sum of a diffuse term and of a coherent term

$$\left(\frac{d\sigma}{d\Omega}\right)_{tot} \propto \sum_X p_X|\mathcal{F}_X|^2 - \left|\sum_X p_X\mathcal{F}_X\right|^2 + \left|\sum_X p_X\mathcal{F}_X\right|^2 S(\mathbf{q}_{\parallel}), \quad (4.3)$$

where

$$S(\mathbf{q}_{\parallel}) = 1 + \int\int_{n\neq m} d^2r_n d^2r_m G(\mathbf{r}_{n,\parallel} - \mathbf{r}_{m,\parallel}) e^{i\mathbf{q}_{\parallel}\cdot(\mathbf{r}_{n,\parallel} - \mathbf{r}_{m,\parallel})} \tag{4.4}$$

is referred to as the total interference function. The second approximation, known as the local monodisperse approximation (LMA),[30] assumes that the cross section is the incoherent summation of the intensities from domains characterized by a single type of particle. This reverts to consider $Y=X$ with $p_Y=1$ in Eq. (4.2). One obtains

$$\left(\frac{d\sigma}{d\Omega}\right)_{tot} \propto \left(\sum_X p_X |\mathcal{F}_X|^2\right) S(\mathbf{q}_{\parallel}). \tag{4.5}$$

The scattered intensity appears as the average of the square of the form factor of the particles times the function $S(\mathbf{q}_{\parallel})$.

For a disordered distribution of particles with an average inter-island distance D, the maxima of $S(\mathbf{q}_{\parallel})$ will be located at $q_{\parallel}$ values multiple of $2\pi/D$. The more cumulative the disorder is, the more the maxima of the function $S(\mathbf{q}_{\parallel})$ are attenuated with increasing $q_{\parallel}$. The intensity on the CCD camera generally appears in the form of only two spots (see Fig. 1), the maxima in these spots being at the average distance $2\pi/D$ from specular position. The shape of the spot gives back the average particle shape through the terms $\mathcal{F}_X$. The spatial extension along horizontal and vertical directions is roughly inversely proportional to the average lateral size $2R$ and height H of the particles. The distribution of intensity of the form factor may shift significantly the position of the GISAXS maxima.[31,32] The DA model, at main variance with the LMA model, is known to generate additional diffuse scattering towards small angles.[31]

On the basis of the paracrystal theory,[33,34] the following one-dimensional (1D) interference function was systematically used

$$S(q_{\parallel}) = \frac{1-\phi^2}{1+\phi^2-2\phi\cos(q_{\parallel}D)}, \tag{4.6}$$

where $\phi=\exp(-q_{\parallel}^2\omega^2/2)$ is the Fourier transform of the probability distribution $p(x)$ of the first neighbor distance D, chosen itself as Gaussian with a half width at half maximum equal to $\sqrt{2\ln 2}\omega$. In the paracrystal model, the neighbors of a given particle are placed sequentially in the vicinity of the nodes of a regular lattice with parameter D. The probability for a particle to be displaced from lattice site increases gradually with its distance from the central particle.

B. Morphological features as stemming from GISAXS

Some experimental GISAXS patterns recorded during the growth of silver on the Zn and on the O surfaces are displayed in Fig. 4. In each case, the distance between the two intensity lobes decreases continuously with increasing coverage. This means that islands coalesce, and this from the very beginning of the growth. The homothetic shrinkage of the intensity observed in the Zn case is indicative of the increase of both the in-plane diameter and the height of the islands. In the O case, the second-order lobes observed along the surface normal direction for Ag thicknesses higher than 0.4 nm, suggest the formation of clusters with a high diameter/height aspect ratio and a well-defined top facet. The second-order lobes correspond indeed to interferences between the waves scattered by the island/support interface and the waves scattered by the top facets. Because of the epitaxial relationship, this top facet is of (111) orientation. The GISAXS analysis is performed using the LMA model on the basis of intensity cuts of the two-dimensional (2D) pattern, either perpendicular [$I(\alpha_f)$ at fixed δ_f] or parallel [$I(\delta_f)$ at fixed α_f] to the surface plane. One generally begins the analysis with two cuts at the positions of maximum intensity (see Fig. 5), that is at $\alpha_f \simeq \alpha_c$ and at $\delta_f \simeq \delta_c$, where δ_c is the relevant angle for $q_y \simeq 2\pi/D$. By use of Eq. (2.1), one obtains the related intensity variations $I(q_z)$ (at fixed q_y) and $I(q_y)$ (at fixed q_z). An overview of such intensity lines for the two surfaces is given at different Ag coverages in Fig. 6. Other cuts (at least 4 as a whole) are then considered to refine the models. The data were fitted using the dedicated program ISGISAXS,[31,35] based on χ^2 minimization and with which several island shapes may be tested, together with various size distributions. In all cluster models investigated, the distribution of the in-plane radius R and of the height H has been chosen as Gaussian with a half width at half maximum given by $\sigma_X\sqrt{2\ln 2}$, where $X=R$ or H. Note the two distributions were always found uncorrelated from each other.

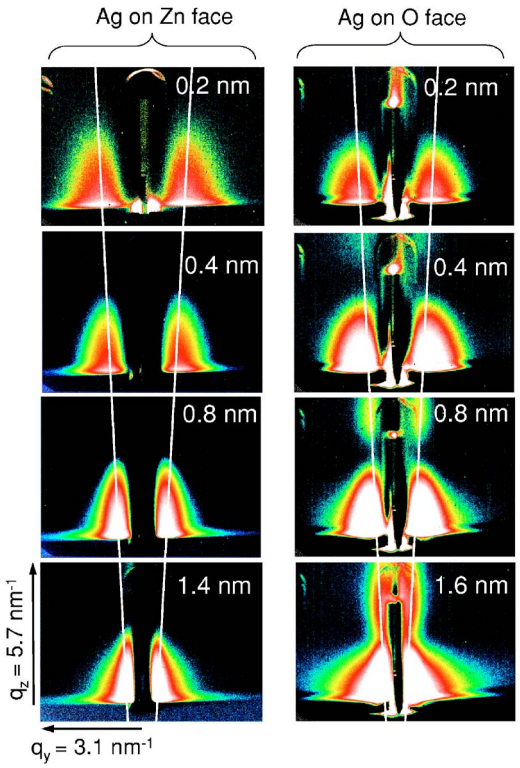

FIG. 4. (Color online) *In situ* GISAXS measurements during Ag deposition on the Zn0(0001) Zn-terminated surface (left column) and on the the Zn0($000\bar{1}$) O-terminated one (right column). The images displayed in logarithmic color scales correspond to an angular aparture of $[-1.9°, 2.3°]$ for δ_f and of $[-0.4°, 3.4°]$ for α_f. Correspondence in reciprocal space units is shown aside.

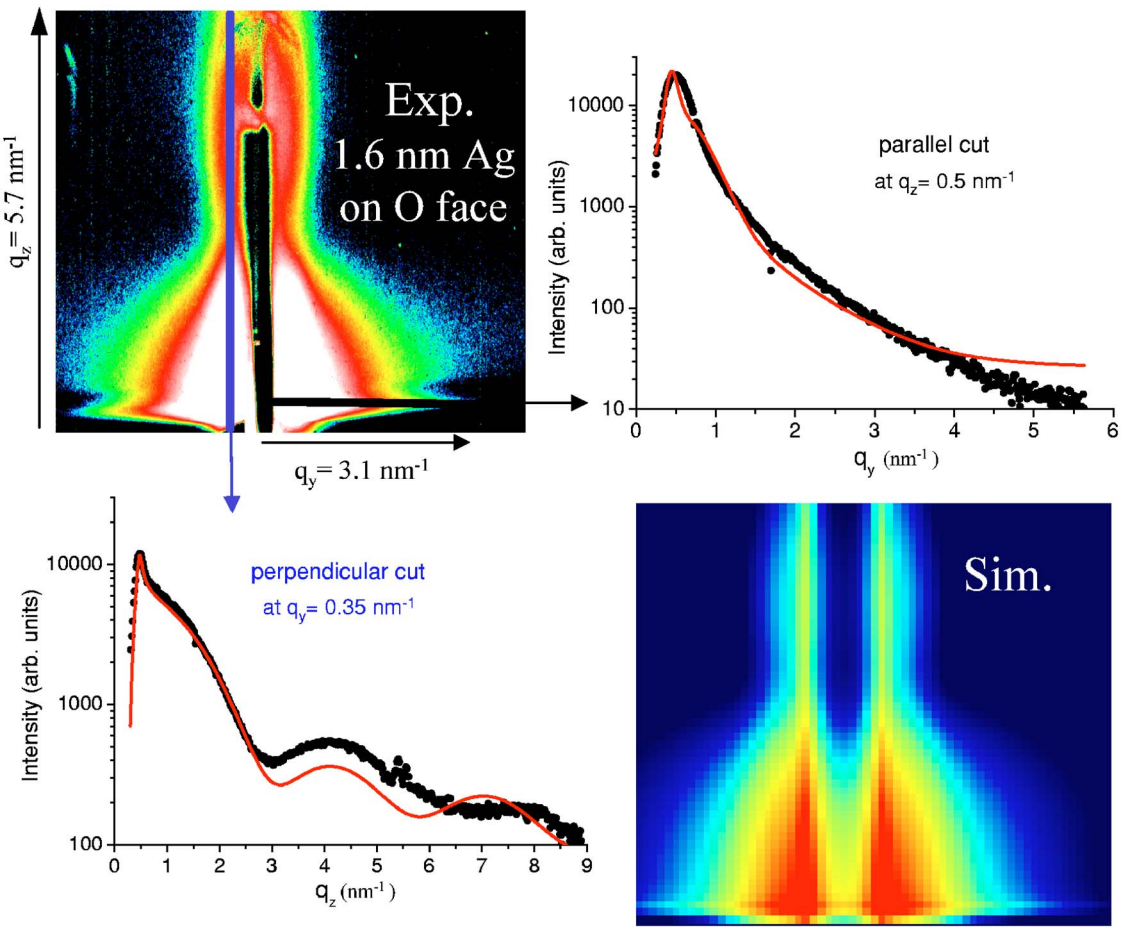

FIG. 5. (Color online) The experimental (top left) and best-fit simulated (bottom right) 2D GISAXS images corresponding to a Ag deposited amount of 1.6 nm on the O face. Perpendicular and parallel cuts of the experimental (simulated) 2D image, at position of maximum intensity, are shown using small circles (solid line). The model used for simulation (hexagonal clusters) is discussed in Secs. IV B 2 and IV C 1

1. Trends in the growth mode of the silver film

The details of the GISAXS analysis depend on the choice of the cluster shape, but general trends should show up whatever model is used. To feature this, a rapid analysis was first performed on the basis of islands with cylinder shape. The interisland distance D increases with coverage on either basal termination, whereas the island diameter and height evolve quite differently. On the ZnO(0001)-Zn face, the height of the Ag clusters raises continuously with coverage, pointing to a 3D growth mode. However, the width σ_R of the in-plane radius distribution dramatically increases with Ag coverage. At and above thickness of 2.4 nm, the relative half-width σ_R/R reaches unphysical values higher than 1. Usually, values of 0.3–0.4 are found for that kind of films.[32] This shows that the assumption of cylindrical shapes is inadequate to model the case. On the contrary, cylinders are convenient for describing the growth of Ag on the O face. On this surface, the cluster height remains almost constant in the 0.2–1.6 nm coverage range. This is a hint that on ZnO(000$\bar{1}$)-O, Ag islands grow preferentially laterally, the spreading of silver being higher than on the Zn face. On both O and Zn surfaces, and as a confirmation of the GIXD results, the islands appear to be formed of about five Ag layers in the early stages of the growth. A puzzling observation is that, for deposited amounts higher than 1.4 nm, the cluster height is close to the average thickness as deduced from the quartz microbalance, whereas the surface fraction Θ covered by silver, as derived from R and D, stays quite low (for a uniform distribution of monosized cylinders, $\Theta = \pi R^2/D^2$).

2. GISAXS pattern symmetry and scatterer shapes

In a second step, the GISAXS data were fitted by using more appropriate shapes of model clusters, accounting for the in-plane symmetry of the substrate and that of the scattering. The patterns in Fig. 4 were obtained with the x-ray beam along the in-plane $[010]_{ZnO}$ axis ($\Omega = 0°$). On the O face, similar patterns were recorded after rotation of the sample around the normal direction by steps of 30° from 0° to 360°. On the Zn face, for deposited amounts ranging between 1.0 and 3.4 nm, the patterns collected with $\Omega = 30°, 90°$ sensitively differ from those obtained with $\Omega = 0°, 60°$. The in-plane scattering is concentrated towards lower q values while the out-of-plane scattering does not show any visible change, as seen in Fig. 7 which displays the perpendicular and parallel cuts at $\delta = \delta_c$ and $\alpha_f = \alpha_c$, respec-

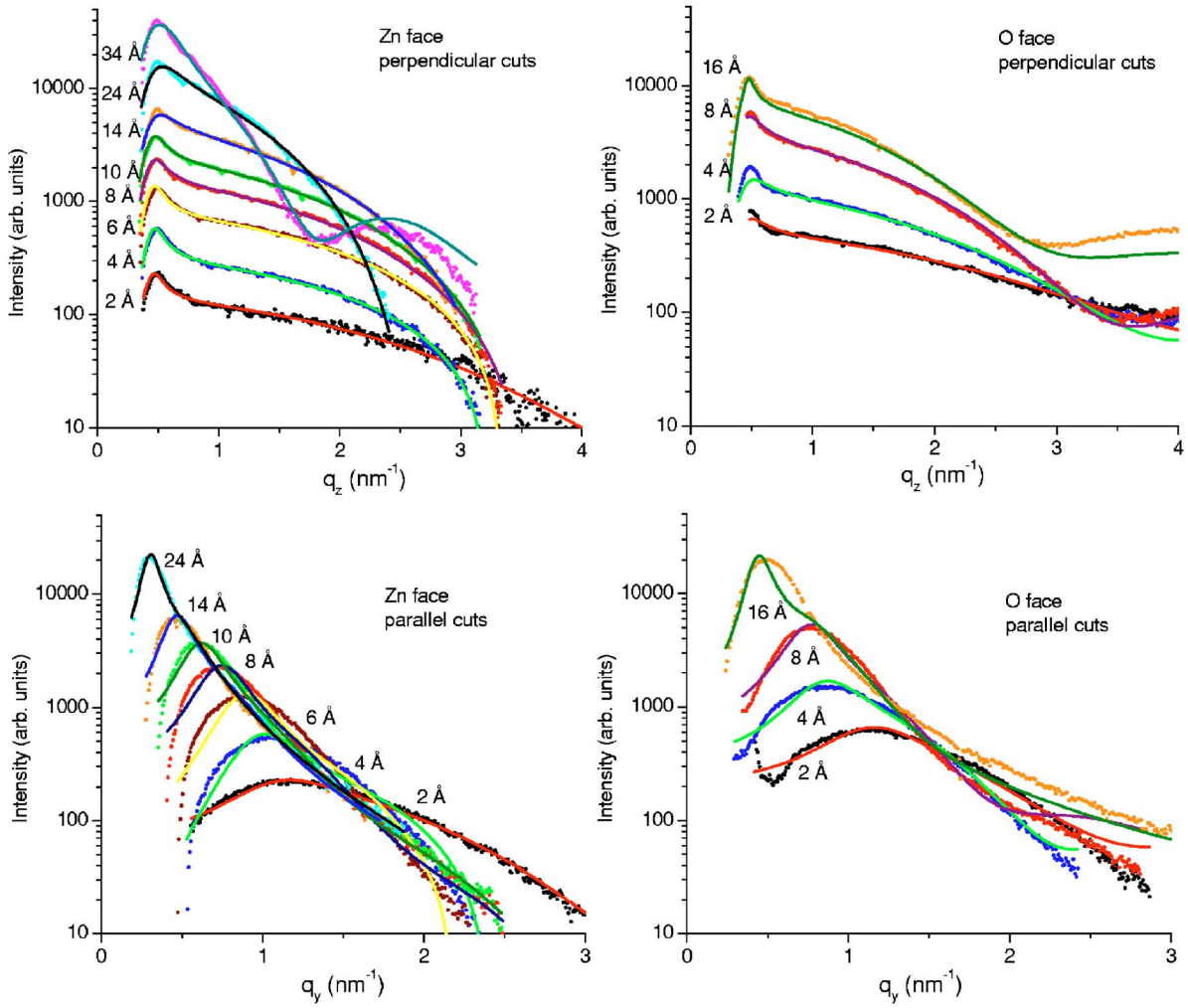

FIG. 6. (Color online) Typical perpendicular and parallel cuts, at positions of maximum intensity, of the 2D GISAXS patterns, for various Ag coverages on the Zn and on the O terminated surface. The cut of experimental pattern is shown as circles, the fit as solid line. The models used for simulation are discussed in Secs. IV B and IV C. Note the big difference in dynamics between intensity profiles collected at low and high coverages. This has precluded the use of a unique color scale over the GISAXS patterns shown in the present work.

tively, of the images recorded on the 3.4-nm-thick Ag film using different sample orientations.

In ZnO, the symmetry of a single (0001) atomic plane is 6 mm, while the symmetry of a set of two (0001) Zn and O successive planes is 3 m. This is why (0001)-oriented bulk ZnO has a 3 m symmetry. The simplest particle shapes compatible with the threefold and sixfold symmetries are triangular or hexagonal prisms. GIXD measurements[16] show that the overall surface symmetry of ZnO is raised from 3 m to 6 mm, due to $c/2$ steps which lead to two types of terraces in equal proportion, each terrace exhibiting 3 m symmetry. In a top view, the down terrace is rotated by 180° (or by 60°) with respect to the up terrace. Assuming a single type of polyhedron on each terrace, one needs at least two polyhedrons rotated by 180° (or 60°) to model the real system. The hexagonal shape is invariant by such rotation, contrary to the triangular shape. For the Zn face, the A_6 axis in GISAXS (invariance after a $2\pi/6$ rotation) may be explained either by triangular clusters with two orientations (see in Fig. 8 the polyhedrons 1, 2 rotated from each other by 180°) or by hexagonal clusters with a single orientation. For the O face, the A_{12} axis in GISAXS requires either four triangular clusters (rotated from each other by 30°) or two hexagonal clusters (rotated from each other by 30°).

All these configurations were tested. In addition, the possible inclination of the lateral faces of the clusters by an angle α with respect to the surface was considered. The triangular and hexagonal prisms become a truncated tetrahedron and a truncated sixfold cone, respectively. The true particle shape may differ from these perfect polyhedrons. In particular, hexagonal particles built with two different side lengths as well as triangular clusters with truncated ends may be anticipated. However, calculation constraints in the GISAXS simulation (see Appendix B) and the multiplication of fit parameters prevent us from considering over complicated geometries. For the same reasons, we did not consider any distribution function for the basis angle α. This being settled, it turns that the GISAXS patterns of the Zn face are best fitted by considering truncated tetrahedrons with a single orientation on each terrace, while the patterns of the O face are best fitted by considering truncated sixfold cones

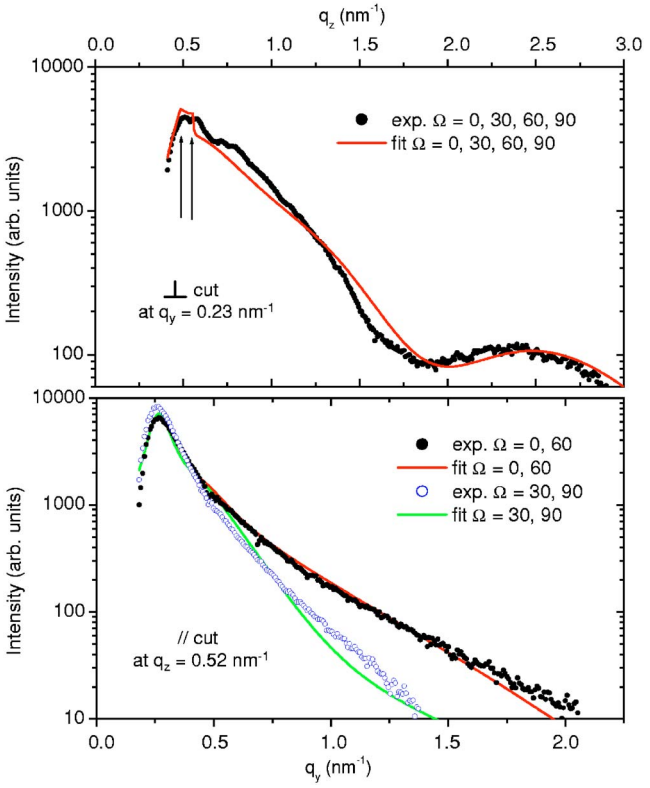

FIG. 7. (Color online) Perpendicular (upper panel) and parallel (lower panel) cuts of the 2D GISAXS images, corresponding to 3.4 nm of Ag deposit on the Zn surface, and recorded for different values (given in degrees) of the in-plane angle Ω between the $[010]_{ZnO}$ axis and the incident x-ray beam. The model is discussed in Secs. IV B 2 and IV C 2. The two maxima (see arrows) observed near $q_z \simeq 0.5$ nm^{-1} result from x-ray reflection at the vacuum/ZnO and Ag/vacuum interfaces.

with two orientations (0 and 30°). The schematic views in Fig. 8 summarize the present findings.

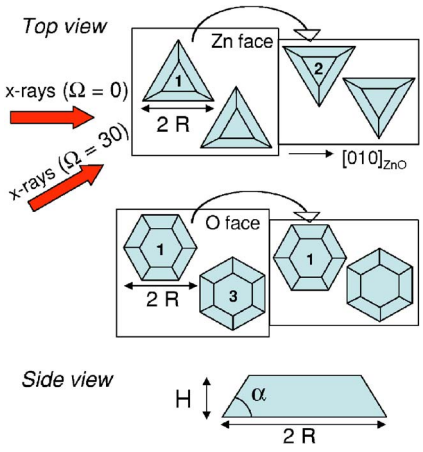

FIG. 8. (Color online) The geometry of polyhedrons used for simulation of GISAXS. Each surface (Zn or O) is presented with two top terraces, turned from each other by 180° around the surface normal. In the Zn case, a single orientation occurs on top of a given terrace whereas two orientations occur in the O case.

About the Zn face, we outline that hexagonal clusters are clearly inadequate for reproducing the differences in the $\Omega = 0°$ and $\Omega = 30°$ patterns. The Ag cluster shape is thus related to the specific symmetry of a terrace, as it results from at least two Zn and O atomic layers. Differently, in the O case, the terrace symmetry is overpassed since two types of clusters develop on each terrace. Consistently, scanning tunneling microscopy (STM) of the bare surfaces has given evidence of triangular ZnO islands and holes on the ZnO(0001)-Zn surface, and of big hexagonal holes on the ZnO(000$\bar{1}$)-O surface.[27] The peculiar terrace topography of the Zn surface is likely determining the shape of the silver particles on that face. The different island geometries observed on the Zn-terminated and on the O-terminated surfaces can be viewed as an indirect consequence of the healing mechanism of the surface polarity.

C. Growth mode of silver on the polar ZnO surfaces

1. The ZnO(000$\bar{1}$)-O face

For the Ag/ZnO(000$\bar{1}$)-O films, the results of data analysis in terms of hexagonal islands are reported in Table I and in Fig. 9 (see also the simulated GISAXS pattern of Fig. 5). In addition to the values of α, $2R$, σ_R/R, H, D, ω derived from the fits, the values of $H/2R$, Θ, t^c have been incorporated in Table I. It is recalled that Θ is the ZnO surface fraction covered by silver as calculated from R, D, ω, and that t^c is the equivalent thickness calculated from R, H, D, according to $t^c = \langle V \rangle / D^2$ where $\langle V \rangle$ is the average volume of a cluster. The H value remains almost constant for Ag deposited amounts between 0.2 and 1.6 nm, while the in-plane island size $2R$ increases. Such enhanced lateral growth of the islands should lead to a progressive coverage of the surface. However, the average island separation D increases much faster than $2R$. Hence, as already found with the crude cylinder model, Θ decreases continuously. The parameters found for a deposited amount of 1.6 nm lead to a value of t^c which is by one order of magnitude too small. Also, the coherent domain size derived from GIXD (6.0 nm) is higher than $2R$ (4.64 nm).

A way to reconcile these apparently conflicting data is to assume the formation by coalescence of (i) large particles whose GISAXS contribution is mostly hidden by the beam stop and (ii) complex faceted wormlike cluster shapes escaping any simple description. As the coverage increases, following the well-known Babinet principle in classical optics, the x-ray GISAXS scattering is better modeled by a continuous thick layer with holes. A specific treatment was thus undertaken, the difference with island scattering coming from the multiple reflection-refraction processes (see Appendix A). X-ray multiple reflection refraction by both the silver-vacuum interface and the silver-ZnO interface, before or/and after the scattering event, are taken into account in the DWBA calculation of the form factor, whereas the simple scheme of supported islands involves the vacuum-ZnO interface alone (see Fig. 11 in Appendix A).

The hole-related morphological parameters (hexagonal shapes were preserved) are given in Table I for Ag deposited

TABLE I. Morphological parameters extracted from the GISAXS analysis of the Ag/ZnO(000$\bar{1}$)-O interface, using hexagonal shape in the island or hole formalism. $\alpha, R, \sigma_R/R, H, D, \omega$ are, respectively, the basis angle, island radius, Gaussian relative radius deviation, height, interisland mean distance, and fluctuation of paracrystalline separation. Are also given the particle $H/2R$ ratio, the surface coverage Θ, the equivalent thickness t^c, as calculated from the shape and spatial distribution parameters.

O face-Hexagonal polyhedrons									
Ag(nm)	α(deg)	$2R$(nm)	σ_R/R	H(nm)	D(nm)	ω(nm)	$H/2R$	Θ	t^c(nm)
Island formalism									
0.2	49±5	2.68	0.245	1.86	4.2	2.1	*0.69*	*0.38*	*0.11*
0.4	55±5	2.76	0.245	2.15	4.9	1.75	*0.78*	*0.29*	*0.11*
0.8	66±3	3.92	0.17	1.98	7.45	2.1	*0.50*	*0.25*	*0.30*
1.6	62±3	4.64	0.29	2.21	13.15	3.6	*0.48*	*0.12*	*0.16*
Hole formalism									
0.8	61±3	4.08	0.14	1.92	7.65	2.1		*0.75*	*1.60*
1.6	60±3	4.68	0.28	2.12	13.2	3.6		*0.88*	*1.95*

amounts of 0.8 and 1.6 nm. They keep close to those found previously by assuming a growth of Ag islands. The 1.6-nm-thick Ag film is correctly described by a 1.9 nm continuous film with holes. As for the 0.8-nm-thick film, both hole and island models give inadequate values for the calculated equivalent thickness t^c. At that coverage, the morphology likely lies between the extreme limits of isolated islands or isolated holes. Last, the basis angle α is found close to the value expected (54.7°) in the case of (001) side facets. Notably, the description of the 1.6 nm Ag/ZnO(000$\bar{1}$)-O film in terms of a continuous layer with holes nicely compares with atomic force microscopy (AFM) images recorded on the same system.[36] These images show large clusters of constant height and a corrugation profile consistent with the assumption of a Ag film with holes.

2. The ZnO(0001)-Zn face

The parameters related to the Ag growth on ZnO(0001)-Zn are given in Table II. Some simulated patterns are displayed in Fig. 10. As seen in Fig. 9, the striking result compared to the Ag/ZnO(000$\bar{1}$)-O case is (i) the increase in both the height H and in-plane size $2R$ of the islands, (ii) the higher increase of $2R$ with respect to D, and (iii) the linear dependence of the separation distance D between islands as a function of size $2R$. Indeed, the parameters R and D appear correlated all along the growth (see the inset in Fig. 9). It is worth to note that the $H/2R$ height-to-width ratio of 0.28 found in the 0.8–1.0 nm range leads to an overall shape (Fig. 8) which looks close to that observed by *in situ* transmission electron microscopy (TEM), for Cu nanocrystals dispersed on ZnO powder under reducing atmosphere.[37]

The surface fraction covered by silver Θ hardly increases with the Ag deposited amount as estimated by the microbalance (from 0.13 to 0.25 for Ag amounts of 0.2 and 3.4 nm, respectively). This might correspond to a poor wetting of the surface by silver, but such interpretation is questioned by the evolution of the equivalent thickness t^c calculated from the fit-derived parameters. The t^c-to-deposited amount ratio decreases from 35% at the beginning of the growth to 13% at

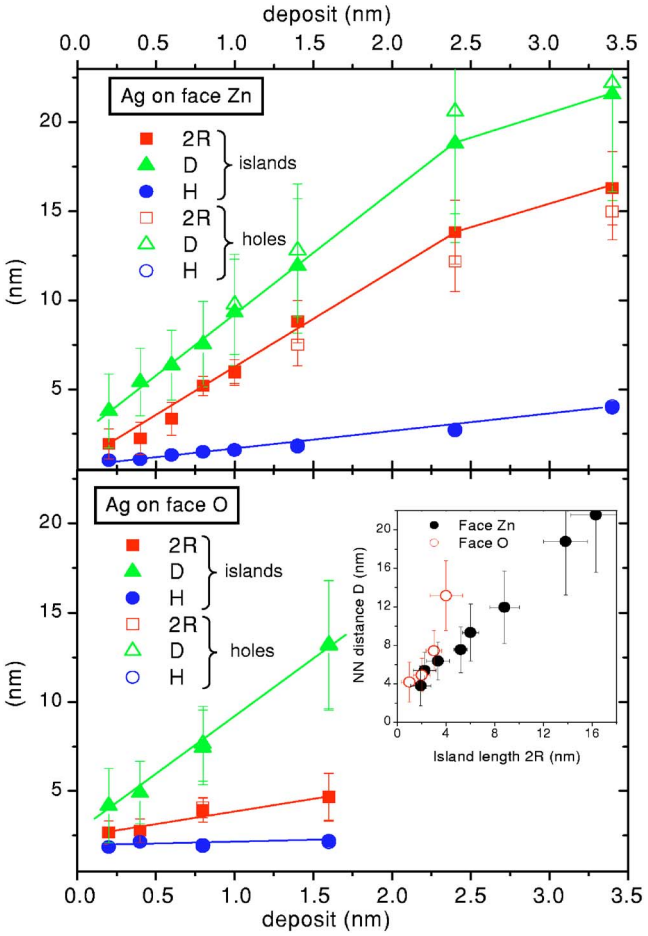

FIG. 9. (Color online) The evolution of island lateral size $2R$ (full squares), height H (full circles), lateral average spacing D (full triangles), as a function of Ag deposit, for the two polar ZnO surfaces, and as deduced from the GISAXS data analysis. The values found assuming the scattering is produced by holes are incorporated in the figure using open symbols. They keep close to those related to islands. The inset displays the nearest neighbor (NN) distance D as a function of island length.

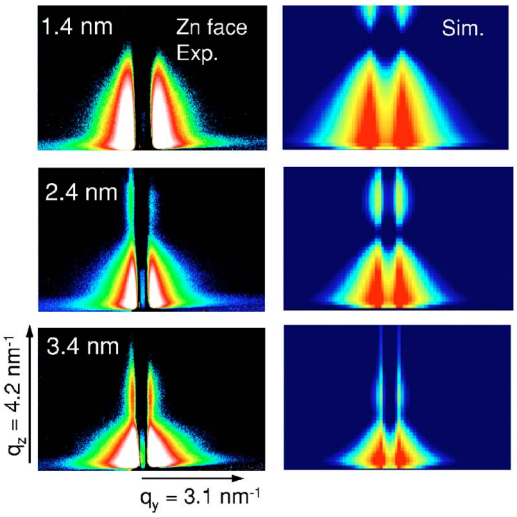

FIG. 10. (Color online) Experimental (left) and simulated (right) 2D GISAXS images corresponding to different Ag deposits on the Zn face.

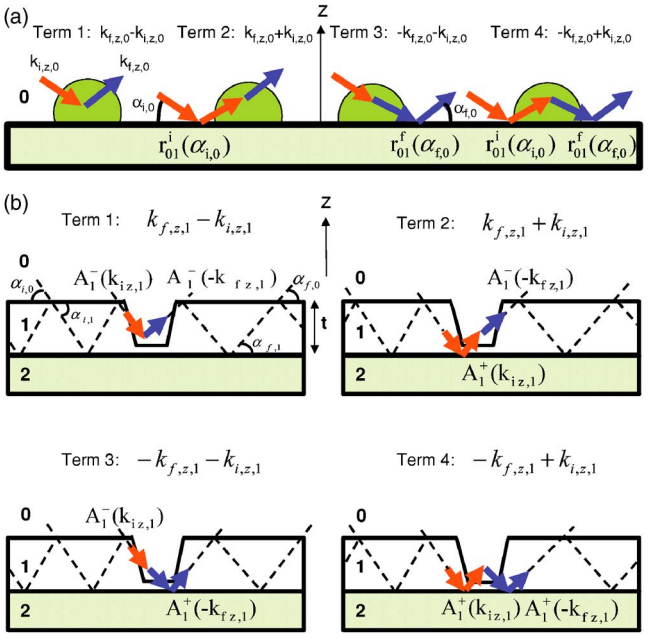

FIG. 11. (Color online) Schematic representation of the four scattering events involved in the DWBA form factor of an island [Eq. (A11)] or of a hole in a layer [Eq. (A12)]. In each situation, the effective perpendicular wave vector transfer is given as well as the involved weighting amplitudes (see text).

3.4 nm. A decrease of the sticking coefficient upon increasing the surface fraction covered by silver is unlikely for a deposition performed at room temperature. Therefore, it is consistent to assume that, beyond a given Ag coverage, GISAXS scattering is (at least partly) generated by holes between the islands, and to model the system by a continuous film with holes, in the same way as for the O-terminated face.

For the higher Ag deposited amounts, the hole scattering scheme leads to calculated equivalent thicknesses in agreement with the values derived from quartz microbalance measurements (see Table II). For intermediate coverage, things are less clear, and it is difficult to specify the moment at which hole scattering prevails with respect to island scattering. On the Zn face, because arguments can be found to favour either island or hole model, it is realistic to assume that the two entities coexist in close proportion in the Ag coverage range under study. As a matter of fact, the nearest neighbor distance D increases with the island (hole) size $2R$ according to: $D=1.3\times 2R$. The proportionality between the two parameters, without any disruption in the full coverage range examined, supports the assumption that correlated islands as well as correlated holes coexist on the surface, with the same average size. The hole height-to-width ratio (about

TABLE II. Same parameters as for Table I but with triangular shape for islands or holes on the ZnO(0001)-Zn face.

Zn face-Triangular polyhedrons									
Ag(nm)	α(deg)	$2R$(nm)	σ_R/R	H(nm)	D(nm)	ω(nm)	$H/2R$	Θ	t^c(nm)
Island formalism									
0.2	69±20	1.92	0.44	1.03	3.8	2.05	*0.38*	*0.13*	*0.07*
0.4	77±15	2.24	0.41	1.12	5.4	1.9	*0.48*	*0.10*	*0.07*
0.6	87±15	3.34	0.28	1.31	6.35	1.95	*0.39*	*0.13*	*0.16*
0.8	84±15	5.20	0.10	1.49	7.55	2.4	*0.29*	*0.21*	*0.28*
1.0	81±15	6.00	0.11	1.60	9.3	3.0	*0.27*	*0.18*	*0.25*
1.4	59±10	8.80	0.14	1.86	11.95	3.8	*0.21*	*0.24*	*0.28*
2.4	52±10	13.80	0.13	2.74	18.8	5.55	*0.20*	*0.24*	*0.37*
3.4	50±10	16.30	0.13	3.97	21.6	6.0	*0.24*	*0.25*	*0.47*
Hole formalism									
1.0	84±15	5.94	0.12	1.62	9.8	2.8		*0.83*	*1.38*
1.4	75±10	7.50	0.16	1.78	12.8	3.7		*0.85*	*1.56*
2.4	63±10	12.18	0.14	2.69	20.6	5.75		*0.85*	*2.42*
3.4	60±10	14.98	0.10	4.07	22.2	6.1		*0.80*	*3.63*

0.25) keeps close to the island $H/2R$ ratio found with the 0.8 nm deposit. Nevertheless, the 3.4-nm-thick Ag film covers a significant fraction of the ZnO surface, as evidenced by the total reflection of x rays at the vacuum/Ag interface. Indeed, two maxima are featured in the intensity scattered along the surface normal direction at angles near α_c^{ZnO} and α_c^{Ag} (see Fig. 7) which demonstrate the occurrence of a flat silver surface in addition to the trivial ZnO surface.

The basis angle α is not determined with accuracy, possibly because of actual shapes differing for the perfect triangles used in the simulation. It is found to evolve between the two angles of 70.5° and 54.7° which correspond to $(11\bar{1})$ and (001) side facets, respectively. The two types of facets have been observed by TEM (Ref. 37) for copper, with apparent preferential development for the (001) orientation.

V. DISCUSSION

Despite the significant differences between the Ag/ZnO(0001)-Zn growth and the Ag/ZnO$(000\bar{1})$-O one, the growth proceeds on the two surfaces via oriented Ag clusters which coalesce in the early stages and in which no strain could be detected by x-ray analysis. Contrary to other metal/oxide systems whose misfit results in strained islands, up to release through a network of interfacial dislocations,[8] the Ag/ZnO system, with a lattice mismatch of −11%, leads to (111) Ag islands in bulklike state. Those islands are azimuthally oriented and show flat top terraces. A similar behavior is observed for Cu/basal ZnO planes, whose lattice mismatch is of −21%.[16] The stabilization of the Ag particles is understandable if one considers coincidence cells at the metal (111)/ZnO(001) interface. A quasiperfect coincidence may be found by superimposing a 9×9 Ag cell on an 8×8 ZnO cell. The misfit is then +0.1%. By comparison, the misfit is −1.8% in the case of a 5×5 Cu cell superimposed on a 4×4 ZnO one. It is interesting to notice that the smaller diameter deduced from GISAXS for the Ag(111) crystallites on ZnO$(000\bar{1})$-O is close to 9 times the silver parameter (see the $2R$ values for a thickness of 0.2 nm).

Concerning the growth mode, the main observations are (i) the formation of flat-top silver clusters on both O-terminated and Zn-terminated ZnO polar surfaces (as in the case of Cu/ZnO)[14] that allows the modeling of the system in the high coverage range by a continuous silver film with holes instead of isolated clusters and (ii) the better spreading on the O surface than on the Zn surface. The Ag/ZnO behavior observed herein contrasts with the very poor wetting by silver of wide band gap oxide surfaces, as it was characterized by *in situ* optical reflectivity on MgO(100) (Ref. 38) and α-$Al_2O_3(0001)$.[39] In the case of the ZnO$(000\bar{1})$-O surface, the constant height of the Ag clusters is consistent with an enhanced lateral growth and thus a high metal/oxide sticking coefficient favoring the increase of the Ag/ZnO interface instead of the increase of metal facets. In the present work, it is not possible to determine the critical coverage[14] since the very first observation which has been made concerns already seven layers thick clusters. However, this first observation gives an upper limit of 0.38 for this parameter. In the case of Ag/ZnO(0001)-Zn, a similar reasoning leads to an upper limit of 0.13 for the critical coverage. The two values are consistent, both in their magnitude and in their hierarchy (the O face is better covered than the Zn face), with those determined for copper, 0.5 (Ref. 40) and 0.35 (Ref. 15) on the O and Zn faces, respectively. On the Zn surface, a constant height-to-width ratio $H/2R$ about 0.25 is inferred for the triangularly shaped Ag crystallites. This as well as the parallel increase of the cluster diameter and of the intercluster distance are indicative of diffusion-mediated capture of deposited adatoms, resulting in a strong correlation between island size and separation.[41,42] The larger the island is, the larger the island-free region around it. Here again, it is in favor of a sticking coefficient weaker than in the O case. Last, the preferred triangular versus hexagonal shape adopted by the Ag nanocrystals on ZnO(0001)-Zn, and which may be related to the specific topography (triangular bumps or holes) of this surface as it results from polarity, enlighten us on the importance of template morphology.

The origin of the formation of flat-top metal clusters on the basal planes of ZnO is an important issue, as well as the understanding of the difference in behavior between the O-terminated and Zn-terminated faces. Density-functional calculations regarding Cu adsorption on the two polar ZnO surfaces have given evidence of a higher adhesion on the O surface,[17] in agreement with the expected ionic (metallic) character of the bonding between noble metal atoms and oxygen (zinc) ions. Meyer and Marx[17] have connected the binding energy to the way the polarity of the clean surfaces is cancelled. They argue that the binding energy decreases as soon as the bands of the oxide surface are filled by the 4*s* electrons of copper and suggest that the switching from 2D islands (islands with a monoatomic thickness) to 3D clusters (as soon as the second layer appears) at the critical coverage could be driven by thermodynamics, not only by kinetics.[14] However, this theoretical treatment was done under the assumption of an ideally strained Cu (111) layer, whereas copper[16] as well as silver (present work) grow epitaxially with their own lattice parameter. Also, the authors have considered a full Cu monolayer and have ignored the particular topography of the Zn surface as it is driven by polarity cancellation. Finally, the lack of local registry between silver or copper metals and zinc oxide, indicates that the short-range Ag-ZnO bonding is likely not the main component of the interfacial energy. Because (i) charge transfer from silver to oxide is generally reduced (same as gold) and (ii) the existence of dipole at the surface of the oxide possibly enhance the metal/oxide image interaction, long range forces (van der Waals and image interactions)[43] might also play a role in the spreading of silver on ZnO.

VI. CONCLUSION

The growth of silver at room temperature on the two polar $(000\bar{1})$-O and (0001)-Zn surfaces of ZnO has been studied *in situ* by GIXD and GISAXS. On both surfaces, silver forms nanoclusters with well-defined top facets, in (111) epitaxy with $[10\bar{1}]$Ag$\|$[100]ZnO. Importantly, the Ag clusters crys-

tallize with their intrinsic bulk parameter, without any detectable strain, and this even at the very beginning of the growth.

Significant differences are found concerning the morphology of the films. GISAXS data demonstrate that triangular islands develop on the Zn face whereas the O face leads to hexagonal shapes. This behavior is connected to the specific topography of the polar ZnO surfaces. As for the film growth, the present GISAXS analysis has rapidly to deal with isolated clusters plus coalesced particles with large diameter or shape escaping simple description. The Ag films at high coverage (above 1 nm) were thus modeled by continuous layers with holes in it. On the O surface, Ag clusters grow laterally while their height stays constant, so that GISAXS is nicely represented by using first the island model then the hole model. On the Zn face, a mixture of clusters and holes with similar shapes and in close proportion is inferred.

Silver spreads better on the ZnO$(000\bar{1})$-O surface than on the ZnO(0001)-Zn surface, as clearly evidenced by the fractions of the surface that are covered by silver for a given deposited amount as well as by the way Ag clusters grow, i.e., mostly laterally on the O surface and both in height and in diameter on the Zn surface. The good spreading of silver on the basal ZnO planes, in particular on the O-terminated surface, likely follows an initial 2D growth up to a significant critical coverage, a behavior which compares with that of Cu/ZnO. Such spreading, which can be unambiguously demonstrated herein by the small angle scattering GISAXS study, contrasts with the growth of silver on alumina or magnesium oxide surfaces, which involves isolated clusters with low aspect ratios.

APPENDIX A: DIFFUSE SCATTERING CROSS SECTION OF ISLANDS OR HOLES: FORM FACTOR TREATMENT

The aim of this appendix is to recall the scattering form factor of an island[29] on a surface and derive that of a hole in a layer within the formalism of the distorted wave born approximation. These two morphologies are the two extreme limits encountered during an heteroepitaxial growth. In small angle scattering, the atomic structure of matter can be safely ignored; only the variation of the mean electronic density has to be accounted for through the average local index of refraction $n(\mathbf{r})$. As for x-rays $n(\mathbf{r})=1-\delta-i\beta$ is very close to one ($\delta\sim\beta\sim10^{-5}$), the polarization effects can be neglected and the propagation equation for the wave field $\Psi(\mathbf{r})$ is reduced to a scalar one[44]

$$[\nabla^2+k_0^2n^2(\mathbf{r})]\,\Psi(\mathbf{r})=0, \tag{A1}$$

where $k_0=2\pi/\lambda$ is the vacuum wave vector and λ the x-ray wavelength. The distorted wave born approximation[29,45–53] is a perturbative formalism applied on the Helmoltz equation Eq. (A1) in order to get the scattering cross section. Defining by n_j the index of refraction of medium j, where the indexes $j=0,1,2$ refer to vacuum, layer (or islands) and substrate, respectively, $(n_0=1, n_1=1-\delta_1-i\beta_1, n_2=1-\delta_2-i\beta_2)$, the local index of refraction is written as

$$n^2(\mathbf{r})=n_j^2(z)-\delta n^2(\mathbf{r})=n_j^2(z)-\delta n_g^2\sum_n S_n(\mathbf{r})\otimes\delta(\mathbf{r}-\mathbf{r}_{\parallel,n}), \tag{A2}$$

where, in the case of islands on a bare substrate: $\delta n_g^2=1-n_1^2$ and in the case of holes in a continuous layer of thickness t: $\delta n_g^2=n_1^2-1$. $S_n(\mathbf{r})$ is the shape function of the island or the hole n (one inside, zero outside) located at the $\mathbf{r}_{\parallel,n}$ position and $\otimes$ is the folding product.

The starting point consists in evaluating the so-called Fresnel wave fields for flat interfaces $\Psi_F(\mathbf{r},\mathbf{k})$ (Ref. 53) in vacuum in the case of islands

$$\Psi_F(\mathbf{r},\mathbf{k})=\psi_0e^{-i\mathbf{k}_\parallel\cdot\mathbf{r}_\parallel}[A_0^+e^{ik_{z,0}z}+e^{-ik_{z,0}z}], \quad \text{where } z>0 \tag{A3}$$

and inside the layer in the case of holes

$$\Psi_F(\mathbf{r},\mathbf{k})=\psi_0e^{-i\mathbf{k}_\parallel\cdot\mathbf{r}_\parallel}[A_1^+e^{ik_{z,1}z}+A_1^-e^{-ik_{z,1}z}], \quad \text{where } -t<z<0. \tag{A4}$$

$\mathbf{k}_\parallel$ is the wave vector component parallel to the substrate while the perpendicular component is given through the Snell–Descartes law: $k_z=-\sqrt{k_0^2-n^2(z)k_\parallel^2}$. The amplitudes $A_j^\pm$ of the upwards and downwards propagating waves in medium j are given by the matching conditions at each interface through the classical Fresnel coefficients of reflection $r_{i,j}$ and transmission $t_{i,j}$ between media i,j,

$$r_{i,j}=r_{i,j}(k_{z,i})=\frac{k_{z,i}-k_{z,j}}{k_{z,i}+k_{z,j}}, \quad t_{i,j}=t_{i,j}(k_{z,i})=\frac{2k_{z,i}}{k_{z,i}+k_{z,j}}. \tag{A5}$$

For a bare substrate

$$A_0^+=A_0^+(k_{z,0})=r_{0,1}, \tag{A6}$$

while for a flat layer

$$A_1^-=A_1^-(k_{z,1})=\frac{t_{0,1}}{1+r_{0,1}r_{1,2}e^{2ik_{z,1}t}}, \quad A_1^+=A_1^+(k_{z,1})=\frac{t_{0,1}r_{1,2}e^{2ik_{z,1}t}}{1+r_{0,1}r_{1,2}e^{2ik_{z,1}t}}. \tag{A7}$$

Within the theory of collisions in quantum mechanics,[54] the T-matrix approach for scattering between the states $\mathbf{k}_i$ and $\mathbf{k}_f$ gives the incoherent scattering cross section

$$\left(\frac{d\sigma}{d\Omega}\right)_{inc}=\frac{k_0^4}{16\pi^2}\left|\int\Psi_F(\mathbf{r},\mathbf{k}_f)\,\delta n^2(\mathbf{r})\Psi_F(\mathbf{r},\mathbf{k}_i)d\mathbf{r}\right|^2. \tag{A8}$$

Only the amplitudes of the Fresnel fields $\Psi_F(\mathbf{r})$ in vacuum [Eq. (A3), $z>0$] for the island, and inside the layer [Eq. (A4), $-t<z<0$] for the hole, respectively, are relevant for the evaluation of the DWBA particle form factor through Eq. (A8). The translation invariance along the interface [expressed through the exponential prefactor in Eqs. (A3) and (A4) and the folding product of Eq. (A2)] allows to separate the particle (island or hole) scattering cross section $(d\sigma/d\Omega)_{par}$ and the interference between waves scattered by

different particles. The interference effects between scatterers and their average along the particle size distribution parameters were developed in Sec. IV A. The particle cross section reads

$$\left(\frac{d\sigma}{d\Omega}\right)_{par} = \frac{k_0^4}{16\pi^2}|\delta n_g^2|^2 \left| \int \Psi_F(\mathbf{r},\mathbf{k}_f) S(\mathbf{r}) \Psi_F(\mathbf{r},\mathbf{k}_i) d\mathbf{r} \right|^2. \tag{A9}$$

The Fresnel wave fields expressions Eqs. (A3) and (A4) show that four different scattering events need to be considered with different scattering wave vector transfers $q_{sc,z} = \pm k_{i,z,(01)} \pm k_{f,z,(01)}$ that are associated to a scattering from an upwards or downwards to upwards or downwards propagating wave. This is illustrated in Fig. 11. It is thus worth noticing that $q_z = k_{f,z,0} - k_{i,z,0}$ in vacuum is not sufficient to fully define the scattering process and that the involved wave vector for holes is the one inside the layer $k_{(i,f),z,1}$ and not in vacuum $k_{(i,f),z,0}$. The particle cross section can be written as

$$\left(\frac{d\sigma}{d\Omega}\right)_{par} = \frac{k_0^4}{16\pi^2}|\delta n_g^2|^2 |\mathcal{F}(\mathbf{q}_\parallel, k_{i,z,0}, k_{f,z,0})|^2, \tag{A10}$$

where for an island

$$\begin{aligned}\mathcal{F}(\mathbf{q}_\parallel, k_{i,z,0}, k_{f,z,0}) = {} & F(\mathbf{q}_\parallel, k_{f,z,0} - k_{i,z,0}) + A_0^+(-k_{f,z,0}) F(\mathbf{q}_\parallel, -k_{f,z,0} \\ & - k_{i,z,0}) + A_0^+(k_{i,z,0}) F(\mathbf{q}_\parallel, k_{f,z,0} + k_{i,z,0}) \\ & + A_0^+(k_{i,z,0}) A_0^+(-k_{f,z,0}) F(\mathbf{q}_\parallel, -k_{f,z,0} + k_{i,z,0})\end{aligned} \tag{A11}$$

and for a hole

$$\begin{aligned}\mathcal{F}(\mathbf{q}_\parallel, k_{i,z,0}, k_{f,z,0}) = {} & A_1^-(k_{i,z,1}) A_1^-(-k_{f,z,1}) F(\mathbf{q}_\parallel, +k_{f,z,1} - k_{i,z,1}) \\ & + A_1^+(k_{i,z,1}) A_1^-(-k_{f,z,1}) F(\mathbf{q}_\parallel, +k_{f,z,1} + k_{i,z,1}) \\ & + A_1^-(k_{i,z,1}) A_1^+(-k_{f,z,1}) F(\mathbf{q}_\parallel, -k_{f,z,1} - k_{i,z,1}) \\ & + A_1^+(k_{i,z,1}) A_1^+(-k_{f,z,1}) F(\mathbf{q}_\parallel, -k_{f,z,1} + k_{i,z,1}).\end{aligned} \tag{A12}$$

The amplitudes $A_j^\pm$ are given for both cases by Eqs. (A6) and (A7), respectively. $F(\mathbf{q})$ stands for the actual particle form factor, i.e., the Fourier transform of its shape

$$F(\mathbf{q}) = \int_{S(\mathbf{r})} e^{i\mathbf{q}\cdot\mathbf{r}} d\mathbf{r}. \tag{A13}$$

For an island, each term is multiplied by the reflection coefficient $A_0^+ = r_{0,1}$ of the incident or scattered wave on the bare substrate. In the hole case, the weights [Eq. (A7)] include either a transmission term at the vacuum-layer interface $r_{0,1}(k_{(i,f),z,1})$ or a reflection term at the layer-substrate interface $r_{1,2}(k_{(i,f),z,1})$, modulated by a Fabry–Pérot interference term $1 + r_{0,1}(k_{(i,f),z,1}) r_{1,2}(k_{(i,f),z,1}) e^{2ik_{(i,f),z,1}t}$ inducing layer thickness interference fringes. As observed experimentally on some GISAXS patterns, these weighting coefficients produce a double Yoneda peak at $\alpha_f \simeq \alpha_c$, one linked to the substrate, the other one to the overlayer. To conclude, it is clear that these two extreme morphological cases give an oversimplified view of the growth process but lead to tractable scattering cross section. In particular, a continuous transition from island to hole case is expected with complicated intermediate morphologies for which the DWBA perturbative formalism is expected to breakdown.

APPENDIX B: FORM FACTOR EXPRESSIONS

The Fourier transform of the shape depicted in Fig. 8 can be calculated analytically

- truncated tetrahedron

$$\begin{aligned}F_{te}(\mathbf{q},R,H,\alpha) = {} & \frac{H}{\sqrt{3}q_x(q_x^2 - 3q_y^2)} e^{iq_z R \tan(\alpha)/\sqrt{3}} [-(q_x \\ & + \sqrt{3}q_y)\mathrm{sinc}(q_1 H) e^{iq_1 L} + (-q_x \\ & + \sqrt{3}q_y)\mathrm{sinc}(q_2 H) e^{-iq_2 L} + 2q_x \,\mathrm{sinc}(q_3 H) e^{iq_3 L}],\end{aligned}$$

$$q_1 = \frac{1}{2}\left[\frac{\sqrt{3}q_x - q_y}{\tan(\alpha)} - q_z\right], \quad q_2 = \frac{1}{2}\left[\frac{\sqrt{3}q_x + q_y}{\tan(\alpha)} + q_z\right], \quad q_3 = \frac{1}{2}\left[\frac{2q_y}{\tan(\alpha)} - q_z\right],$$

$$L = \frac{2\tan(\alpha)R}{\sqrt{3}} - H, \tag{B1}$$

- truncated prism with sixfold symmetry

$$\begin{aligned}F_{co6}(\mathbf{q},R,H) = {} & \frac{4\sqrt{3}}{3q_y^2 - q_x^2} \int_0^H [q_y^2 R_z^2 \,\mathrm{sinc}(q_x R_z/\sqrt{3})\mathrm{sinc}(q_y R_z) \\ & + \cos(2q_x R_z/\sqrt{3}) \\ & - \cos(q_y R_z)\cos(q_x R_z/\sqrt{3})] e^{iq_z z} dz,\end{aligned}$$

$$R_z = R - z/\tan(\alpha),$$

$$H/R < \tan(\alpha). \tag{B2}$$

For holes, a mirror symmetry perpendicular to the z axis has to be applied before using the previous formulas.

[1] H. J. Freund, Surf. Sci. **500**, 271 (2002).

[2] J. Jupille, Surf. Rev. Lett. **8**, 69 (2001).

[3] W. Hirschwald, *Zinc Oxide: Properties and Behaviour of the Bulk, the Solid/Vacuum and Solid/Gas Interface, Material Science*, Vol. 7 (E. Kaldis North Holland, Amsterdam, 1981).

[4] R. Zhang, A. Ludviksson, and C. Campbell, Surf. Sci. **289**, 1 (1993).

[5] E. Valkonen, B. Karlsson, and C. Rissing, Sol. Energy **32**, 2121

(1984).
[6] http://www-cenerg.ensmp.fr/ease/advanced_glazing.
[7] C. Henry, Surf. Sci. Rep. **31**, 231 (1998).
[8] G. Renaud, Surf. Sci. Rep. **32**, 1 (1998).
[9] M. Valden, X. Lai, and D. W. Goodman, Science **281**, 1647 (1998).
[10] C. T. Campbell, S. C. Parker, and D. E. Starr, Science **298**, 811 (2002).
[11] S. Roberts and R. Gorte, J. Chem. Phys. **93**, 5337 (1990).
[12] W. T. Petrie and J. M. Vohs, J. Chem. Phys. **101**, 8098 (1994).
[13] P. V. Radulovic, C. S. Feigerle, and S. H. Overbury, J. Phys. Chem. **104**, 3028 (2000).
[14] C. T. Campbell, Surf. Sci. Rep. **27**, 1 (1997).
[15] J. Yoshihara, S. Parker, and C. Campbell, Surf. Sci. **439**, 153 (1999).
[16] N. Jedrecy, S. Gallini, M. Sauvage-Simkin, and R. Pinchaux, Phys. Rev. B **64**, 085424 (2001).
[17] B. Meyer and D. Marx, Phys. Rev. B **69**, 235420 (2004).
[18] J. R. Levine, J. B. Cohen, Y. W. Chung, and P. Georgopoulos, J. Appl. Crystallogr. **22**, 528 (1989).
[19] A. Naudon and D. Thiaudière, J. Appl. Crystallogr. **30**, 822 (1997).
[20] T. Metzger, I. Kegel, R. Paniago, and J. Peisl, J. Phys. D **32**, A202 (1999).
[21] G. Renaud, R. Lazzari, C. Revenant, A. Barbier, M. Noblet, O. Ulrich, F. Leroy, J. Jupille, Y. Borenstzein, C. R. Henry, J-P. Deville, F. Scheurer, J. Mane-Mane, and O. Fruchart, Science **300**, 1416 (2003).
[22] N. Jedrecy, J. Appl. Crystallogr. **33**, 1365 (2000).
[23] R. Baudoing-Savois, M. De Santis, M. Saint-Lager, P. Dolle, O. Geaymond, P. Taunier, P. Jeantet, J. Roux, G. Renaud, and A. Barbier, Nucl. Instrum. Methods Phys. Res. B **149**, 213 (1999).
[24] G. Renaud, M. Ducruet, O. Ulrich, and R. Lazzari, Nucl. Instrum. Methods Phys. Res. B **222**, 667 (2004).
[25] N. Jedrecy, M. Sauvage-Simkin, and R. Pinchaux, Appl. Surf. Sci. **162–163**, 69 (2000).
[26] O. Dulub, U. Dielbold, and G. Kresse, Phys. Rev. Lett. **90**, 016102 (2003).
[27] O. Dulub, L. Boatner, and U. Diebold, Surf. Sci. **519**, 201 (2001).
[28] A. Guinier and G. Fournet, *Small-Angle Scattering of X-Rays* (Wiley, New York, 1955).
[29] M. Rauscher, R. Paniago, H. Metzger, Z. Kovats, J. Domke, H. D. Pfannes, J. Schulze, and I. Eisele, J. Appl. Phys. **86**, 6763 (1999).
[30] J. S. Pedersen, J. Appl. Crystallogr. **27**, 595 (1994).
[31] R. Lazzari, J. Appl. Crystallogr. **35**, 406 (2002).
[32] C. Revenant, F. Leroy, R. Lazzari, G. Renaud, and C. R. Henry, Phys. Rev. B **69**, 035411 (2004).
[33] R. Hosemann and S. N. Bagchi, *Direct Analysis of Diffraction by Matter* (North-Holland, Amsterdam, 1962).
[34] R. Millane and J. Eads, Acta Crystallogr., Sect. A: Found. Crystallogr. **A56**, 497 (2000).
[35] R. Lazzari, ISGISAXS can be downloaded with an user guide from: http://www.esrf.fr/computing/scientific/joint_projects/IsGISAXS/isgisaxs.htm (2002).
[36] R. Lazzari and J. Jupille, Surf. Sci. **482–485**, 823 (2001).
[37] P. Hansen, J. Wagner, S. Helveg, J. Rostrup-Nielsen, B. Clausen, and Topsøe, Science **295**, 2053 (2002).
[38] R. Lazzari, J. Jupille, and Y. Borensztein, Appl. Surf. Sci. **142**, 451 (1999).
[39] R. Lazzari and J. Jupille, Phys. Rev. B **71**, 045409 (2005).
[40] K. H. Ernst, A. Ludviksson, R. Zhang, J. Yoshihara, and C. T. Campbell, Phys. Rev. B **47**, 13782 (1993).
[41] M. C. Bartelt, A. K. Schmid, J. W. Evans, and R. Q. Hwang, Phys. Rev. Lett. **81**, 1901 (1998).
[42] M. C. Bartelt, C. R. Stoldt, C. J. Jenks, P. A. Thiel, and J. W. Evans, Phys. Rev. B **59**, 3125 (1999).
[43] F. Didier and J. Jupille, J. Appl. Phys. **58**, 253 (1996).
[44] S. Dietrich and A. Haase, Phys. Rep. **260**, 1 (1995).
[45] G. H. Vineyard, Phys. Rev. B **26**, 4146 (1982).
[46] S. K. Sinha, E. B. Sirota, S. Garoff, and H. B. Stanley, Phys. Rev. B **38**, 2297 (1988).
[47] V. Holý, J. Kubena, I. Ohlídal, K. Lischka, and W. Plotz, Phys. Rev. B **47**, 15896 (1993).
[48] V. Holý and T. Baumbach, Phys. Rev. B **49**, 10668 (1994).
[49] M. Rauscher, T. Salditt, and H. Spohn, Phys. Rev. B **52**, 16855 (1995).
[50] D. K. G. deBoer, Phys. Rev. B **49**, 5817 (1994).
[51] D. K. G. deBoer, Phys. Rev. B **51**, 5297 (1995).
[52] D. K. G. deBoer, Phys. Rev. B **53**, 6048 (1996).
[53] J. Daillant and A. Gibaud, *X-Ray and Neutron Reflectivity: Principle and Applications*, Lectures notes in physics (Springer, New York, 1999).
[54] A. Messiah, *Quamtum Mechanics* (Dunod, Paris, 1964), Vols. 1–2.